Journal of Materials Chemistry A

High-pressure induced a stable phase of Li2MnSiO4 for an effective poly-anion cathode material from simulations

Journal:	*Journal of Materials Chemistry A*
Manuscript ID	TA-ART-03-2019-003369.R2
Article Type:	Paper
Date Submitted by the Author:	13-Jun-2019
Complete List of Authors:	Wang, Shuo; Peking University, Materials Science and Engineering Liu, Junyi; Peking University, Qie, Yu; Peking University, college of engineer Gong, Sheng; Peking University, Department of Materials Science and Engineering Zhang, Cunzhi; Peking University Sun, Qiang; Peking University, Jena, Purusottam ; Virginia Commonwealth University, Physics Department

High-pressure induced a stable phase of Li_2MnSiO_4 for an effective poly-anion cathode material from simulations

Shuo Wang[a], Junyi Liu[a], Yu Qie[a], Sheng Gong[b], Cunzhi Zhang[a],Qiang Sun [c,d,a,*], and Puru Jena[e]

[a] Department of Materials Science and Engineering, College of Engineering, Peking University, Beijing 100871, China

[b] Department of Materials Science and Engineering， Massachusetts Institute of Technology，Cambridge，MA 02139，USA

[c] Center for Applied Physics and Technology, Peking University, Beijing 100871, China

[d] Key Lab of Theory and Technology for Advanced Batteries Materials, College of Engineering, Peking University, Beijing 100871, China

[e] Department of Physics, Virginia Commonwealth University, Richmond, VA 23284, USA

Abstract

Search for novel cathode materials is of current interest. Among them, Li_2MnSiO_4 shows promise as a cathode material in the poly-anion family due to its structural diversity, abundance, low cost, and high theoretical capacity (330 mAh/g). However, it suffers from low electronic and ionic conductivity, limited reversible capacity, and poor cycling performance. To overcome these deficiencies, using a global structure search in high pressure we find a new phase with a group symmetry of *Cc*, which is the ground-state in pressure of 50Gpa, and remains stable when pressure is released. This new phase exhibits many attractive features such as a high energy density of 612 Wh/kg with a reversible capacity of 170 mAh/g, a high average discharging voltage of 3.6V, improved electronic conductivity, coexistence of anionic and cationic redox, and superior ionic conductivity due to the unique diffusion channels with reduced steric hindrance and coulombic repulsion. All these features endow the new phase of Li_2MnSiO_4 with the potential of high performance for cathode material.

Keywords: Cathode material, Li_4MnSiO_4, High pressure, DFT calculations

1. Introduction

Driven by the need for high-performance Li-ion batteries, extensive studies have been carried out on several classes of cathode materials during the past three decades, including chalcogenides[1], layered oxides[2, 3], spinel oxides[4], olivine phosphates[5], silicates[6], tavorites[7], *etc.* However, transition-metal (TM) layered oxides remain dominant in Li-ion battery industry due to their high voltage, stable cycling performance and mature synthesis technology[8]. However, the intrinsic instability of layered TM-oxides[9] at deep delithiation makes it difficult to achieve high reversible capacity in the derived $LiMO_2$ materials (M = single or combination of Ni, Mn, Co, Fe, Al *etc.*). Therefore, it is highly desirable to explore new cathode materials with enhanced stability and improved energy density.

Recently, the poly-anion family has attracted extensive attention, which shows great structural diversity due to the various structural geometries composed of poly-anion units $(XO_4)^{n+}$ and their derivatives $(X_mO_{3m+1})^{n-}$ (X=P, S, As, Mo, Si etc.)[10]. These materials display great potentials not only as superionic conductors with high ionic conductivity (such as β-, γ-, or LISICON-type solid electrolyte[11]), but also as cathode materials with high voltage and cycling stability (such as olivine phosphate $LiFeO_4$,[5] silicates $Li_2(Fe/Co/Mn)O_4$[12]). This is due to the strong covalent bonding between poly-anion units and MO_x polyhedrons (M=transition metal) that enables the structural matrix to accommodate a wide range of cations for good ion conductivity and to endure the deformation induced by Li intercalation or deintercalation[13]. Among the studied systems, Li_2MSiO_4 (M=transitional metal) is a promising cathode material with a high theoretical capacity[14] (>320 mAh/g). Although M=Fe system is mostly explored, the redox of Fe^{2+}/Fe^{3+} limits the stable cycling capacity to 140 mAh/g which is only half of the theoretical value. Besides, the average voltage platform is relatively low (~2.85V)[15], thus leading to low energy density (480 Wh/kg). Considering the balance between energy density and cost, Mn system is attractive due to its abundance in nature and high voltage and capacity in redox of Mn^{2+}/Mn^{3+} and Mn^{3+}/Mn^{4+}. However, it suffers from structural failure during cycling, poor electronic and ionic conductivity[16]. To further explore Mn-based poly-anion cathode materials, in this study we report a new phase of Li_2MnSiO_4 induced by high pressure.

In fact, as a fundamental thermodynamic variable, pressure is very effective in synthesizing new materials by changing interatomic distances, modifying bonding patterns, reordering the atomic

orbitals, and overcoming chemical reactive barriers for phase transition.[17-20] Recently, many functional materials with outstanding performance are synthesized such as superconductors, superhard materials and high-energy-density materials[21-22] because of developed high-pressure experimental techniques. However, the traditional ways of high-pressure experiments are not efficient for quick exploration due to heavy workload and long experiment period. Crystal-structure searching based first-principles calculation has been proven to be able to accurately predict new materials. In this study, using a global structure search in high pressure we find a new phase of Li_2MnSiO_4 with improved performance.

2. Methods

We first use the CALYPSO[22] (Crystal structure AnaLYsis by Particle Swarm Optimization) package to perform global structure search at 50GPa for stable/metastable phases by sorting energy from first-principles calculation at defined chemical composition (e.g. Li2MnSiO4). Then we perform calculations based on density functional theory (DFT) as implemented in the Vienna Ab Initio Simulation Package (VASP)[23]. Projector augmented-wave (PAW)[24] method with Perdew–Burke–Ernzerhof (PBE) generalized-gradient approximation[25] (GGA) for exchange and correlation potential are used. The energy cutoff of the plane waves is 600 eV, and pseudopotentials of Li ($2s^1$), Mn ($3d^64s^1$), Si ($3s^23p^2$), O ($2s^22p^4$) are used. In consideration of strong correlation effect of Mn, Hubbard U correction[26] (GGA+U scheme) is used in this work, an effective Hubbard U value of 6.0 is adopted for the d orbital of Mn as reported in previous work[27]. Total energy convergence criteria and Hellmann-Feynman force are set to 1×10^{-4} eV and 1.0×10^{-2} eV/Å, respectively, during structural optimization. The smallest allowed spacing between sampled k-points in reciprocal lattice is set as $0.15A^{\circ-1}$.

To confirm the dynamical stability of the structure, we calculate the phonon spectrum using the finite displacement method as implemented in the Phonopy[28]. The convergence criterion for energy is set to 1×10^{-8} eV during the phonon calculations. The thermodynamic stability is confirmed with *ab initio* molecular dynamic (AIMD) simulation using the Nose-Hoover heat bath (NVT) at 500 K within a 2×2×2 supercell (a=b=12.0 Å, c=9.9 Å) containing 128 atoms. The mechanical stability is verified using the criteria for monoclinic phase.[29]

To study the diffusion of Li ions, climbing image-nudged elastic band (CI-NEB)[30] approach is

used to calculate the energy barrier of Li diffusion to adjacent vacancy within the same supercell. AIMD simulations at elevated temperature are carried out to calculate the mean square displacement (MSD) to study collective Li-ion transport according to the formula below[31]:

$$\langle[\vec{r}(t)]^2\rangle = \frac{1}{N}\sum_{i=1}^{N}\left\langle\left[\overrightarrow{r_i}(t + t_0) - \overrightarrow{r_i}(t_0)\right]^2\right\rangle \qquad (1)$$

where $\vec{r}(t)$ is the displacement of the ith Li^+ ion at time *t* and *N* is the total number of Li^+ ions in the system. The diffusion coefficient (*D*) is calculated by fitting to the MSD according to

$$D = \lim_{t\to\infty}\left[\frac{1}{2dt}\langle[\vec{r}(t)]^2\rangle\right] \qquad (2)$$

where *d* is the dimensionality of diffusion and *t* is the elapsed simulation time. The diffusion activation energy is extrapolated according to Arrhenius equation:

$$D = D_0 * \exp\left(-\frac{Ea}{RT}\right) \qquad (3)$$

Where D_0 is the maximal diffusion coefficient, E_a is the activation energy for diffusion, T is the absolute temperature and R is the universal gas constant. More calculation details are shown in SI.

3. Results and discussions

3.1 Structure and stability

We carried out global structural search with chemical formula of Li_2MnSiO_4 at pressure of 50 GPa and find a new ground-state structure, in which the primitive cell contains 16 atoms including two formula of Li_2MnSiO_4 with two equivalent sites for each atom. Its space group is *Cc*, which is different from the existing structures of *Pnma* and *Pmn21*. The detailed lattice parameters and structural geometry are shown in Figure 1 and SI. In comparison with the existing structures observed in experiment (Figure S1), both the Si-O and Mn-O polyhedrons constitute the main structural skeleton but in different ways: firstly, Si has six coordinated oxygens in *Cc* phase but four in *Pnma* and *Pmn21* phases, because high-pressure usually leads to configurations with increased coordination number; secondly, in *Pnma* and *Pmn21* structures, the multivalent cations (Mn, Si) and Li ions distribute alternately in 2D layers (Figure S1) along c-axis as layered rock-salt $LiCoO_2$, while Si-O and Mn-O octahedrons connect to each other with edge sharing along each lattice direction to form consecutive 3D skeletons as shown in Figure 1. Such structural geometry would lead to favorable ionic diffusion as discussed in Section 3.2.

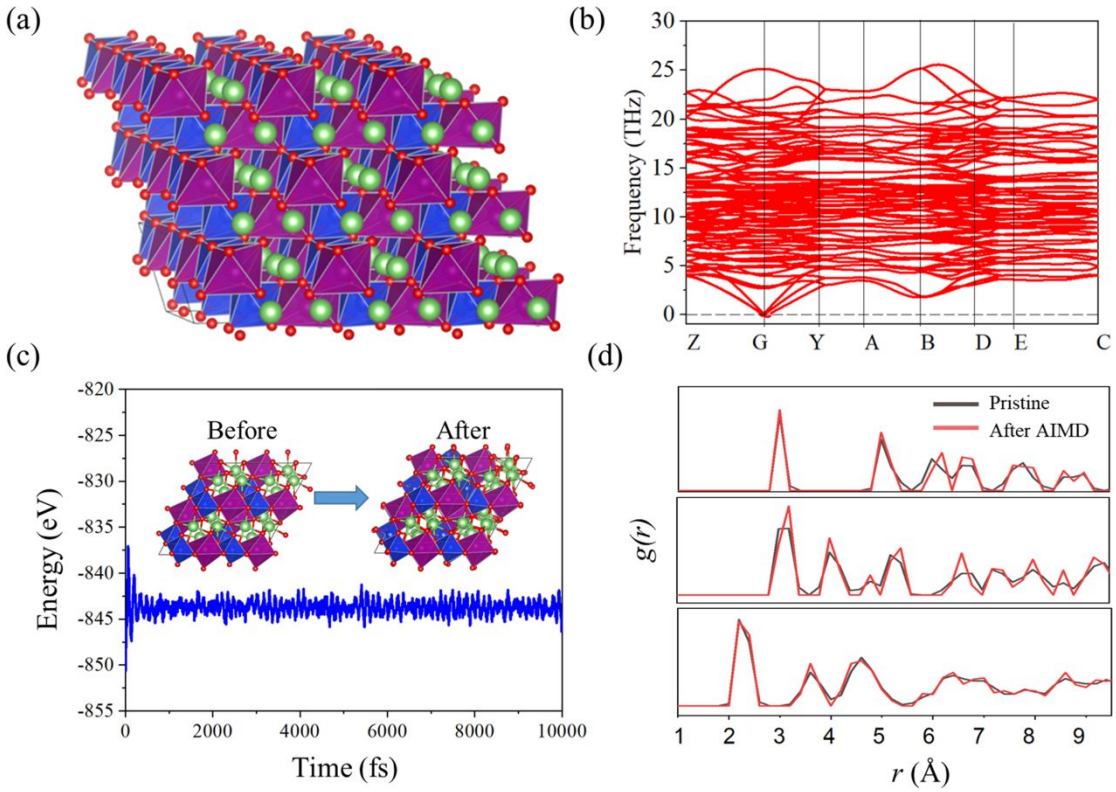

Figure 1. (a) Structural configuration of *Cc* Li_2MnSiO_4 phase and (b) phonon spectra along the high symmetry k-path in the first Brillouin zone, (c) fluctuation of total potential energy with respect to time during AIMD simulation at 500 K, (d) pair correlation function *g(r)* of Mn-Mn, Mn-Si and Mn-O for the structures before and after AIMD.

To explore the effect of pressure, enthalpy difference (ΔH) curves as a function of pressure is plot in Figure 2 according to the equation: $\Delta H = H(X) - H(Ref)$ where *Ref* = *Cc* and *X* = *Pnma, Pmn21*. The results show that the *Pnma* and *Pmn21* structures are most stable phases with quite small (~35 meV/atom) energy difference at ambient pressure, which agrees with the coexistence of two phases during experimental synthesis.[32] However, the ground state inversion happens at the crossing point of 19 GPa, which is much less than the recently reported large-volume high-pressure techniques (90GPa) in experiment[33], suggesting the feasibility of synthesizing this new phase in pressure.[33]

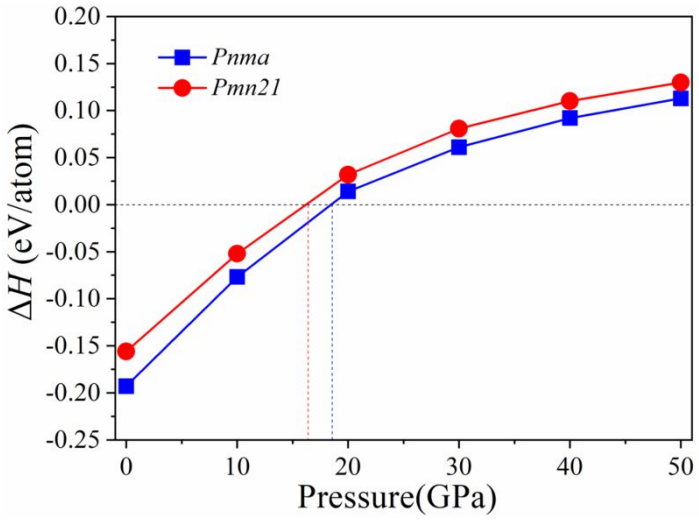

Figure 2. Enthalpy difference [$\Delta H = H(X) - H(Ref)$] changing with pressure (*Ref* = *Cc*, *X* = *Pnma*, *Pmn21*).

To further verify the stability of the *Cc* phase once the applied pressure is removed, the dynamical and thermal stability are evaluated by AIMD and phonon spectrum calculation. The phonon dispersion of *Cc* Li_2MnSiO_4 along high-symmetry k-path in the first Brillouin zone is shown in Figure 1(b). There are no imaginary modes confirming the dynamic stability of this new phase. Besides, AIMD simulation is carried out with a 2×2×2 supercell at 500K in the canonical ensemble. The average total potential fluctuation remains constant with respect to time. Figures 1 and S2 show the structural snapshots and pair correlation functions of Mn-Mn, Mn-Si and Mn-O extracted from initial and final image. After ten-picosecond molecular dynamics simulations, the structural skeleton remains nearly intact without structural breakage or reconstruction, and the pair correlation functions of the initial structure also agree well with those of the final image. All of these results show that the *Cc* phase is thermally and dynamically stable after the release of pressure.

In addition, the mechanical stability is also confirmed according to the criteria of monoclinic phase[29]:

$$C_{11}>0,\ C_{22}>0,\ C_{33}>0,\ C_{44}>0,\ C_{55}>0,\ C_{66}>0,$$

$$[C_{11}+C_{22}+C_{33}+2(C_{12}+C_{13}+C_{23})]>0,$$

$$(C_{33}C_{55}-C_{35}^2)>0,\ (C_{44}C_{66}-C_{46}^2)>0,\ (C_{22}+C_{33}-2C_{23})>0$$

$$[C_{22}(C_{33}C_{55}-C_{35}^2)+2C_{23}C_{25}C_{35}-C_{23}^2C_{55}-C_{25}^2C_{33}]>0$$

$$\{2[C_{15}C_{25}(C_{33}C_{12}-C_{13}C_{23})+C_{15}C_{35}(C_{22}C_{13}-C_{12}C_{23})+C_{25}C_{35}(C_{11}C_{23}-C_{12}C_{13})]-[C_{15}^2(C_{22}C_{33}-C_{23}^2)+C_{25}^2(C_{11}C_{33}-C_{13}^2)+C_{35}^2(C_{11}C_{22}-C_{12}^2)]+C_{55}>0$$

$$g = C_{11}C_{22}C_{33} - C_{11}C_{23}^2 - C_{22}C_{13}^2 - C_{33}C_{12}^2 + 2C_{12}C_{13}C_{23}$$

The detailed elastic stiff constants C_{xy} are listed in Table 1. Clearly, they satisfy the mechanical stability criteria for monoclinic phase. We also calculated the Hill-average Bulk modulus (B_H=123 GPa), shear modulus ((G_H=80 GPa)), and Young's modulus (E_H=197 GPa). The results show that the *Cc* structure is mechanically stronger than the experimental structure *Pnma* (B_H=98 GPa, G_H=68GPa) and *Pmn21* (B_H=100 GPa, G_H=69GPa) given in Materials Project database[34]. All the above results proves it feasible to synthesize the *Cc* phase with assistance of high-pressure and could be stable after pressure release.

Table 1. Elastic stiff constants (GPa) C_{ij} of *Cc* Li_2MnSiO_4 without pressure.

System	C_{11}	C_{22}	C_{33}	C_{44}	C_{55}	C_{66}	C_{12}
	248.8	237.4	246.9	77.9	82.7	83.4	82.5
Cc-Li_2MnSiO_4	C_{13}	C_{23}	C_{15}	C_{25}	C_{35}	C_{46}	
	73.2	67.8	23.4	7.9	-11.6	4.2	

3.2 Li ionic diffusion behavior

To evaluate the ionic mobility, we calculate the energy barriers for Li diffusion with vacancy-filling model in a 2×2×2 supercell using CI-NEB method (Figure 3). The reliability of supercell size is confirmed by the convergence of the results in larger supercell as shown in Figure S4. Since one-dimensional (1D) channels exist along the *a*-axis and *b*-axis (labeled *a*-channel and *b*-channel), we chose five different paths to simulate the diffusion within 1D tunnels (Path A and E) and the shuttling between *a*-channel and *b*-channel (Path B, C, D). Due to different chemical environment, there are two kinds of lithium, which lead to the energy difference between the initial and the end state for some paths. We find that the consecutive diffusion in 1D channels is difficult due to the high barrier of 1.5 eV (Path E), while the shuttling diffusion is more favorable with relatively low barrier of 0.6~0.9 eV. Based on these results, one can expect that these shuttles would connect these 1D channels to construct 3D networks for ionic diffusion. The energy barriers are comparable to other reported metal-oxide cathodes such as Li_xAlO_2 (0.65~1.41 eV)[35], Li_xMnO_3 (0.51~0.84 eV)[36], Li_2FeSiO_4 (0.84~1.76 eV)[37].

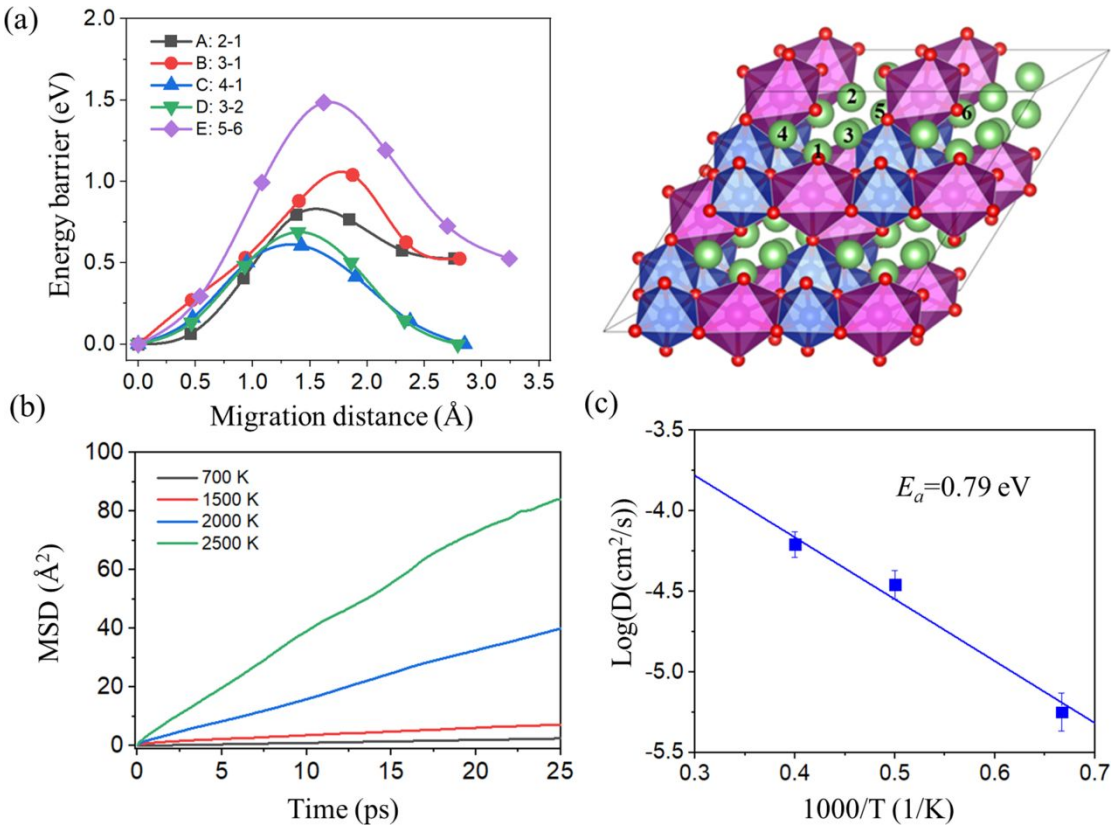

Figure 3. (a) Migration energy barriers in Li_2MnSiO_4 and the illustration of the lithium migration paths. The Li, Mn, Si, O atoms are marked with green, purple, blue and red, respectively. (b) The MSD of diffusive Li atoms from AIMD at temperature from 700K to 2500K. (c) The Arrhenius plots of Li diffusion and extrapolated activation barrier.

The diffusion barrier in *Pmn21* phase is also calculated and is found to be 1.3 eV for Li ion hopping to adjacent vacancy. As mentioned in Section 3.1, different geometries between *Cc* phase and *Pmn21* phase lead to different local configurations for ionic diffusion as shown in Figure 4. In the new *Cc* phase, three Li atoms occupy the cubic vertexes and Li hopping happens through the cubic center. However, when one Li atom at the cubic vertex is replaced by a Si or Mn, the hopping Li ion has to go across the plane due to the stronger coulombic repulsion and steric hindrance between Li ion and Mn, Si atoms. This would also lead to changes in coordinated environment for diffusive Li ion (six-fold to two-fold in *Pmn21* phase, while six-fold to four-fold in *Cc* phase). Such diffusion behaviors affected by cation distribution are also reported in previous work[38]. And our calculation shows that the barrier can be reduced from 1.3 eV (in *Pmn21* phase) to 0.6 eV (Path-C in *Cc* phase). Hence, a higher ionic conductivity is expected in our new phase compared to

experimental structures, which is also observed in AIMD simulation as discussed below.

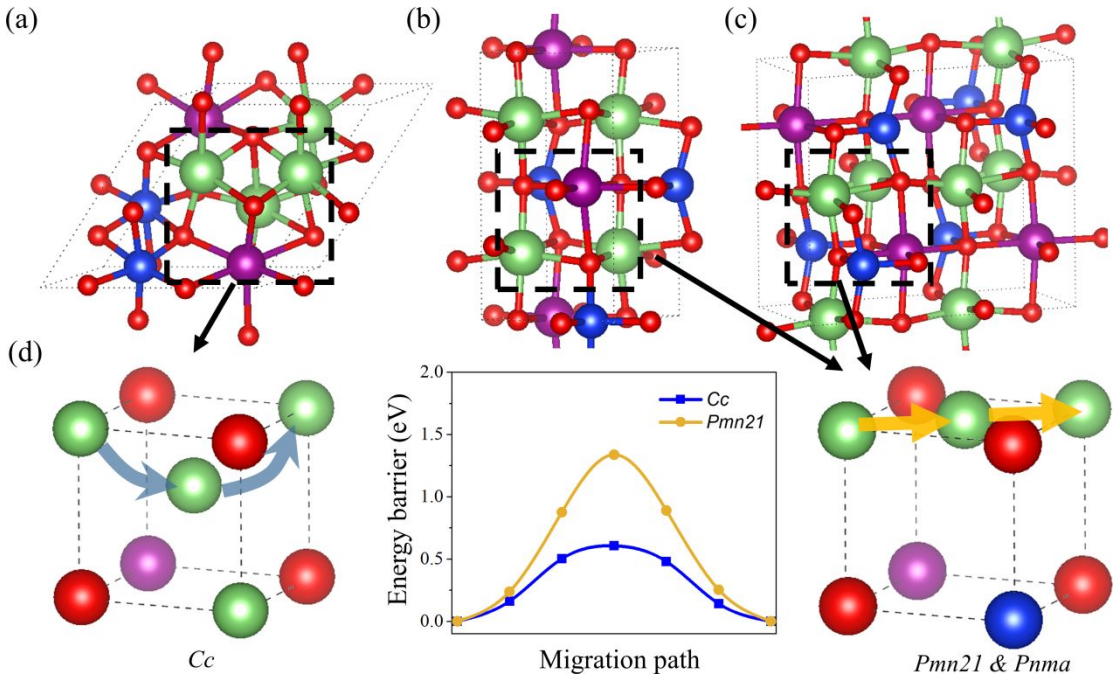

Figure 4. The local structural geometry (dashed box) extracted from (a) *Cc* phase and (b) *Pnm21,* (c) *Pnma* structures. (d) The simulated energy barriers of two phases corresponding to the different ionic diffusion paths (arrowed line),

The AIMD simulations from 700K to 2500K using a 2×2×2 supercell with eight Li vacancies are carried out to further explore the ionic diffusion behavior from the perspective of thermo-kinetics. Elevated temperature is used to accelerate the diffusion process and thermalization over 4-ps is performed with advanced analysis strategy proposed by Mo *et.al*.[39] to reduce the statistical variances from AIMD simulations. The results as illustrated in Figure 3 indicate that Li ions do not show consecutive ionic diffusion behavior until the temperature is above 1500K, and the extrapolated activation energy for ionic diffusion is 0.79 eV which is consistent with CI-NEB results. As a comparison with *Cc* phase, the AIMD simulation at 2000K is carried out for *Pmn21* phase and the MSD results are shown in Figure S5, which suggests that *Cc* phase has faster Li ionic diffusion as expected from the analysis of local structural geometry. And the extrapolated diffusivity *D* for *Cc* phase (2.8×10^{-5} cm^2/s) is 14 times higher than that of *Pmn21* structure ($1.95\times10^{-6}cm^2/s$). Visualization of Li-ion diffusion trajectories at 1500K is shown in Figure S7, which confirms the

expected 3D diffusive channels. The relation between diffusive carrier density and conductivity is explored as shown in Figure S6, which indicates that more vacant carriers are favorable for ionic hopping, thus the conductivity would increases with delithiation.

3.3 Redox reaction and oxygen stability during delithiation

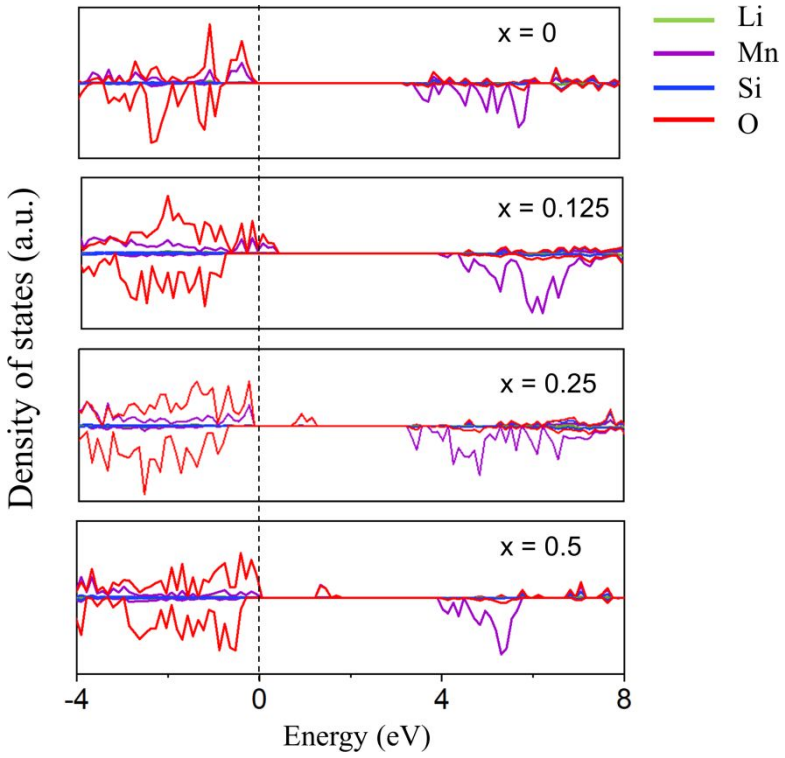

Figure 5. Element-projected density of states (DOS) of $Li_{2(1-x)}MnSiO_4$ at different delithiation condition that x=0, 0.125, 0.25 and 0.5.

Although our calculations proves that the new phase of Li_2MnSiO_4 is intrinsically stable and has superior ionic conductivity, manganese migration and oxygen local displacement occur during AIMD at above 2000K. Actually, structural failure and phase transition are also observed experimentally[40], which raises challenges in structural stability during delithiation. Redox reactions of the TM cations would happen during delithiation that can induce distortion or even structural failure due to strong Jahn-Teller effect. And transition metal is usually considered to be the only source to compensate the charge when Li ions are extracted.[41] To explore the origin of redox reaction and its relation to structural stability in the *Cc* phase during delithiation, the DOS and Bader charge as function of Li concentration are also calculated (Figure 6, Table S2). One can see the

overlap between the states of Mn and O around Fermi level, indicating both covalent and ionic bonding between TM and O atoms, and leading to potential redox competition between Mn and O during delithiation. And the Bader charge results confirm the simultaneous oxidation of Mn and O at the beginning of lithium deintercalation ($x<0.25$ in $Li_{2(1-x)}MnSiO_4$) that valence of Mn increases from +1.55 to +1.74 and O increases from -1.84 to -1.68. But when deep delithiation continues ($x>0.5$ in $Li_{2(1-x)}MnSiO_4$), oxygen become the only redox center that valence of O increase from -1.70 to -1.52 while valence of Mn keeps nearly intact (from +1.90 to +1.94). And the intermediate peak from oxygen in the DOS for delithiated $Li_{2(1-x)}MnSiO_4$ agrees well with the Bader charge analysis. Our results suggest that the capacity is not only provided by redox of Mn but also by the O, and synergistic redox behavior between O and Mn contributes to the capacity synchronously. These results are helpful for better comprehending anionic redox that is not only in Li-excess layered oxides but also in poly-anion system. One thing is that the bandgap narrows down for *Cc* phase while delithiation happens due to the decreased Fermi level and emergent intermediate peak from oxidized oxygen. It is interesting to note that the bandgap narrows down for Cc phase during delithiation due to the Fermi level shift and the emergent intermediate peak from oxidized oxygen. Similar phenomenon is also observed in the band gap evolution from 2.1 eV for $LiCoO_2$ (MP-number: 24850) to 0.0 eV for $Li_{0.5}CoO_2$ (MP-number: 762036) and Molenda *et.al.*'s work.[42]

To estimate the upper limit of reversible capacity, the oxygen release of mostly oxidized oxygen atom in the delithiated supercell simulated. Although oxygen release depends on several factors such as electron redistribution, fracture and reformation of bonding, and dynamical barrier, we only consider the reaction enthalpy as the thermodynamic driving force according to the reaction below**:**

$$Li_2MnSiO_4(s) \rightarrow Li_2MnSiO_{4-y}(s) + \frac{y}{2}O_2(g) \quad (4)$$

Where *E* is the total energy per f.u. To avoid the overestimation of DFT in calculating the binding energy of O_2 molecule[36], we use the following equation:

$$E(O_2) = 2E_{DFT}(H_2O) - 2E_{DFT}(H_2) - 2\Delta E_{exp}(H_2O) \quad (5)$$

And the change of enthalpy (ΔH) is calculated as

$$\Delta H = \frac{Li_2MnSiO_{4-y}(s) + (y/2)E_{O_2} - Li_2MnSiO_4(s)}{y/2} \quad (6)$$

The entropy correction of gas phase O_2 under standard conditions (-TS= 0.63 eV) is also included here in evaluating the Gibbs free energy (ΔG). The positive (negative) reaction enthalpy suggests

that oxygen-release reaction is energetically unfavorable (favorable). The results in Table 1 indicate that more than half of lithium atoms (>170 mAh/g) might reversibly insert in and out without facilitating oxygen release. Furthermore, the Mn displacement to adjacent Li vacancy is also simulated and the results are shown in Table S3. The ΔE is positive for two experimental structures but negative for the *Cc* phase, which suggests the intrinsic mobility of Mn in this high-pressure phase. However, the barrier for Mn displacement is up to 1.48 eV, which explains the stability of structures during AIMD simulation when the temperature is less than 700K.

Table 1. Calculated Gibbs free energy for O_2 release in the ground states of $Li_{2(1-x)}MnSiO_4$ with x= 0.125, 0.25, 0.5, 0.75.

Materials	Concentration	*x=0.125*	*x=0.25*	*x=0.50*	*x=0.75*
$Li_{2(1-x)}MnSiO_4$	ΔG *(eV)*	2.12	1.80	0.90	-1.38

3.4 Voltage platform

Voltage is another key factor to characterize the performance of cathode materials, which determines the energy density in combination with capacity. For a cathode material, the charge/discharge process follows the common half-cell reaction vs. Li/Li+:

$$(x_2 - x_1)\mathrm{Li}^+ + (x_1 - x_2)\mathrm{e}^- + \mathrm{Li}_{X1}\mathrm{MnSiO_4} \leftrightarrow \mathrm{Li}_{X2}\mathrm{MnSiO_4} \qquad (7)$$

The effect of volume, pressure, and entropy is ignored here. The average voltage in the concentration range of $x_1 < x < x_2$ is estimated by calculating the energy difference over parts of the Li composition domain:

$$\mathrm{V} = \frac{E_{\mathrm{Lix_1MnSiO_4}} - E_{\mathrm{Lix_2MnSiO_4}} + (x_2 - x_1)E_{\mathrm{Li}}}{x_2 - x_1} \qquad (8)$$

The key to simulate the voltage curve is to determine the stable intermediate configurations at different Li concentration. Ten structures with different Li distribution at each specific Li concentration ($Li_{2(1-x)}MnSiO_4$: x = 0.125, 0.25, 0.5, 0.75) are constructed. For a given Li-vacancy configuration, the formation energy E_f is calculated as below:

$$E_f(x) = E_{\mathrm{Li2(1-x)MnSiO4}} - xE_{\mathrm{MnSiO4}} - (1-x)E_{\mathrm{Li2MnSiO4}} \quad (9)$$

The energy-favorable structures at different intermediate concentrations are used to calculate voltage profile as shown in Figure 5. The voltage increases from 3.3 V to 4.0 V with continuous delithiation due to the enhanced interaction between poly-anion framework and Li atoms. The whole average voltage is about 3.9 V, which is comparable to the values of 3.9 and 4.2 V for $LiNiO_2$ [43] and $LixMn_2O_4$ [44] , while it is higher than the voltage of anatase-TiO_2 (1.9 V)[45], V_2O_5 (2.8V)[46], and LiFePO4 (3.2V)[47]. However, one should notice that due to the instability of oxygen and Mn as discussed in Section 3.3, the reversible capacity is limited to 170 mAh with an average voltage of 3.6 V, resulting in a high energy density of 612 Wh/kg, and the appropriate voltage platform (<4V) enables better interfacial safety with conventional carbonate solvents.[48]

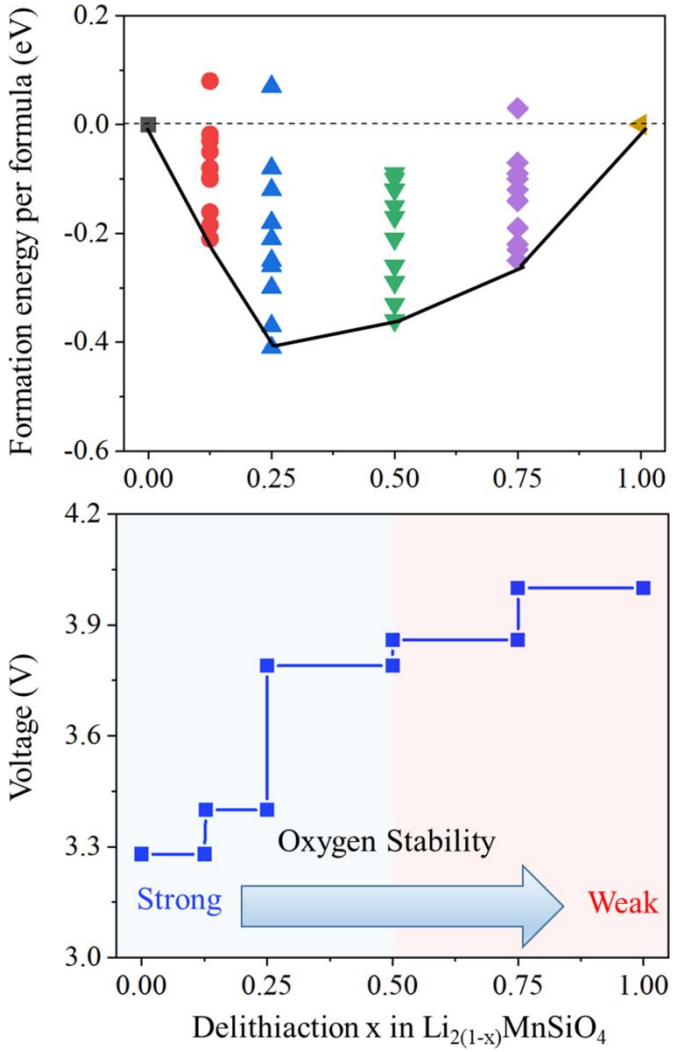

Figure 6. Formation energy of intermediate phases of $Li_{2(1-x)}MnSiO_4$ and the corresponding voltage profile as function of delithiation content (x=0.125, 0.25, 0.5, 0.75, 1.0).

4. Conclusions

In summary, we have found a new phase of Li_2MnSiO_4 in high pressure using global crystal structure search combined with first-principles calculation. Main conclusions are as follows: (1) the new phase with a space group symmetry of *Cc* is feasible to be synthesized as the required pressure is only about 20Gpa, and it remains dynamically, thermally and mechanically stable after the pressure is released; (2) the new phase has 3D channels for Li ions diffusion and shows a high ionic conductivity because of the unique structural geometry; (3) the new phase exhibits a high energy density of 612 Wh/kg with reversible capacity of 170 mAh/g and average voltage of 3.6 V. Moreover, synergetic redox activity from both Mn cations and O anions favors the high capacity. These interesting results not only indicate the potential of the new Li_2MnSiO_4 phase as a high performance cathode, but also the effectiveness of high-pressure synthesis for exploring novel battery materials.

ACKNOWLEDGMENTS

S. W appreciates the financial support from China Scholarship Council. This work is partially supported by grants from the National Key Research and Development Program of China (2016YFB0100200), and from the National Natural Science Foundation of China (21573008 and 21773003). P. J. acknowledges the support by the U.S DOE, Office of Basic Energy Sciences, Division of Material Sciences and Engineering under Award No. DE-FG02-96ER45579. Part of the numerical simulations are performed on the High-Performance Computing Platform of Peking University and High-performance Computing Platform of CAPT.

Reference:

1. D. Murphy and F. Trumbore, *Journal of Crystal Growth*, 1977, **39**, 185-199.
2. S. Wang, J. Liu and Q. Sun, *Journal of Materials Chemistry A*, 2017, **5**, 16936-16943.
3. M.-K. Song, S. Park, F. M. Alamgir, J. Cho and M. Liu, *Materials Science and Engineering: R: Reports*, 2011, **72**, 203-252.
4. S. Patoux, L. Daniel, C. Bourbon, H. Lignier, C. Pagano, F. Le Cras, S. Jouanneau and S. Martinet, *Journal of Power Sources*, 2009, **189**, 344-352.
5. P. S. Herle, B. Ellis, N. Coombs and L. F. Nazar, in *Materials For Sustainable Energy: A Collection of Peer-Reviewed Research and Review Articles from Nature Publishing Group*, World Scientific,

2011, pp. 199-204.
6. C. Masquelier and L. Croguennec, *Chemical Reviews*, 2013, **113**, 6552-6591.
7. T. Mueller, G. Hautier, A. Jain and G. Ceder, *Chemistry of Materials*, 2011, **23**, 3854-3862.
8. T. Ohzuku and Y. Makimura, *Chemistry letters*, 2001, **30**, 744-745.
9. R. Trivedi, *Metallurgical and Materials Transactions A*, 1995, **26**, 1583-1590.
10. Z. Gong and Y. Yang, *Energy & Environmental Science*, 2011, **4**, 3223-3242.
11. P. Knauth, *Solid State Ionics*, 2009, **180**, 911-916.
12. H.-N. Girish and G.-Q. Shao, *Rsc Advances*, 2015, **5**, 98666-98686.
13. J. C. Kim, Massachusetts Institute of Technology, 2013.
14. R. Dominko, M. Bele, A. Kokalj, M. Gaberscek and J. Jamnik, *Journal of Power Sources*, 2007, **174**, 457-461.
15. A. Nytén, A. Abouimrane, M. Armand, T. Gustafsson and J. O. Thomas, *Electrochemistry communications*, 2005, **7**, 156-160.
16. R. Gummow and Y. He, *Journal of Power Sources*, 2014, **253**, 315-331.
17. L. Zhang, Y. Wang, J. Lv and Y. Ma, *Nature Reviews Materials*, 2017, **2**, 17005.
18. M. Miao, *Nature Chemistry*, 2013, **5**, 846-852.
19. E. Zurek, R. Hoffmann, N. W. Ashcroft, A. R. Oganov and A. O. Lyakhov, *Proceedings of the National Academy of Sciences of the United States of America*, 2009, **106**, 17640-17643.
20. S. Wang, J. Liu, Y. Qie, S. Gong, Q. Sun and P. Jena, *Journal of Materials Chemistry A*, 2018, **6**, 18449-18457.
21. A. P. Drozdov, M. I. Eremets, I. A. Troyan, V. Ksenofontov and S. I. Shylin, *Nature*, 2015, **525**, 73.
22. Y. Wang, J. Lv, L. Zhu and Y. Ma, *Physics*, 2010, **82**, 7174-7182.
23. G. Kresse and J. Furthmüller, *Physical review B*, 1996, **54**, 11169.
24. P. E. Blöchl, *Physical Review B*, 1994, **50**, 17953.
25. J. P. Perdew, K. Burke and M. Ernzerhof, *Physical review letters*, 1996, **77**, 3865.
26. H. J. Kulik, M. Cococcioni, D. A. Scherlis and N. Marzari, *Physical Review Letters*, 2006, **97**, 103001.
27. H. Lee, S.-D. Park, J. Moon, H. Lee, K. Cho, M. Cho and S. Y. Kim, *Chemistry of Materials*, 2014, **26**, 3896-3899.
28. A. Togo, F. Oba and I. Tanaka, *Physical Review B*, 2008, **78**, 134106.
29. Z. J. Wu, E. J. Zhao, H. P. Xiang, X. F. Hao, X. J. Liu and J. Meng, *Physical Review B*, 2007, **76**, -.
30. G. Henkelman, B. P. Uberuaga and H. Jónsson, *The Journal of chemical physics*, 2000, **113**, 9901-9904.
31. A. Emly, E. Kioupakis and A. Van der Ven, *Chemistry of Materials*, 2013, **25**, 4663-4670.
32. T. Masese, Y. Orikasa, C. Tassel, J. Kim, T. Minato, H. Arai, T. Mori, K. Yamamoto, Y. Kobayashi and H. Kageyama, *Chemistry of Materials*, 2014, **26**, 1380-1384.
33. S. Zhai and E. Ito, *Geoscience Frontiers*, 2011, **2**, 101-106.
34. A. Jain, S. P. Ong, G. Hautier, W. Chen, W. D. Richards, S. Dacek, S. Cholia, D. Gunter, D. Skinner and G. Ceder, *Apl Materials*, 2013, **1**, 11002.
35. M. M. Islam and T. Bredow, *The journal of physical chemistry letters*, 2015, **6**, 4622-4626.
36. R. Xiao, H. Li and L. Chen, *Chemistry of Materials*, 2012, **24**, 4242-4251.
37. R. B. Araujo, R. H. Scheicher, J. S. de Almeida, A. Ferreira da Silva and R. Ahuja, *Solid State Ionics*, 2013, **247-248**, 8-14.

38. A. Urban, J. Lee and G. Ceder, *Advanced Energy Materials*, 2014, **4**, 1400478.
39. X. He, Y. Zhu, A. Epstein and Y. Mo, *Npj Computational Mathematics*, 2018, **4**, 18.
40. Q. Cheng, W. He, X. Zhang, M. Li and L. Wang, *Journal of Materials Chemistry A*, 2017, **5**, 10772-10797.
41. C. Zhan, Z. Yao, J. Lu, L. Ma, V. A. Maroni, L. Li, E. Lee, E. E. Alp, T. Wu and J. Wen, *Nature Energy*, 2017, **2**, 963.
42. J. Molenda, A. Stokłosa and T. Bąk, *Solid State Ionics*, 1989, **36**, 53-58.
43. C. Ouyang, S. Shi, Z. Wang, X. Huang and L. Chen, *Physical Review B*, 2004, **69**, 104303.
44. Y. S. Meng and M. E. Arroyo-de Dompablo, *Energy & Environmental Science*, 2009, **2**, 589-609.
45. B. J. Morgan and G. W. Watson, *Physical Review B*, 2010, **82**, 144119.
46. X. Rocquefelte, F. Boucher, P. Gressier and G. Ouvrard, *Chemistry of materials*, 2003, **15**, 1812-1819.
47. M. E. Arroyo-de Dompablo, M. Armand, J. M. Tarascon and U. Amador, *Electrochemistry Communications*, 2006, **8**, 1292-1298.
48. D. Aurbach, Y. Talyosef, B. Markovsky, E. Markevich, E. Zinigrad, L. Asraf, J. S. Gnanaraj and H.-J. Kim, *Electrochimica Acta*, 2004, **50**, 247-254.